**ORIGINAL PAPER**

# The Effect of Mn$^{4+}$ and Ni$^{2+}$ Co-substitution Barium Monoferrite: Phase Formation, Raman Analysis, Magnetic Properties, and Microwave Absorbing Property Studies

Ade Mulyawan[1] · Salim Mustofa[1] · Deswita[1] · Raden Andhika Ajiesastra[2] · Wisnu Ari Adi[1]

## Abstract

In this work, to modify the magnetic and microwave absorbing properties of barium monoferrite, Mn$^{4+}$/Ni$^{2+}$ co-substitution barium monoferrite with the nominal composition of Ba$_{0.9}$Sr$_{0.1}$Fe$_{(2-2x)}$(Mn,Ni)$_x$O$_4$ ($0.0 \leq x \leq 0.5$) have been synthesized via solid-state reaction method. Rietveld refinement process was carried out to reveal the structural parameters, bond lengths, and bond angles. The lattice constants showed variation associated to the lattice distortion as evidenced from the fluctuations of the bond angles and bond lengths, the results also in accordance with phonon modes of Raman spectra. The microstructure of the samples obtained from scanning electron microscope (SEM) showed spherical particle size with strong tendency for particles to agglomerate. Magnetic property parameters were obtained from vibrating sample magnetometer (VSM) measurement. It was found that the sample changed its magnetic behavior from hard to soft ferromagnetic due to the Mn$^{4+}$/Ni$^{2+}$ substitution; the field coercivity value was found to decrease by 80.3% with a slight substitution of $x = 0.1$. Moreover, it has been explained on the basis of the Stoner-Wohlfarth equation regarding the relation between field coercivity, saturation magnetization, and magneto-crystalline constant ($K$). In the frequency range of 9–12 GHz, the Mn$^{4+}$/Ni$^{2+}$ substitution made the reflection loss (RL) curve to have a broad feature with multiple attenuation peaks. The RL bandwidth at higher microwave attenuation level (RL $< -16.5$ dB, $\approx 97\%$ attenuation) varied at 1.44 GHz to 1.65 GHz, while the original sample was 0.67 GHz. These features were attributed to the magnetic resonance loss and hysteresis loss which originated from to the natural ferromagnetic resonance. Moreover, The RL minimum was shifted to a lower frequency due to the decreasing $K$ value in the substituted samples.

**Keywords** Barium monoferrite · Tetravalent and divalent substitution · Rietveld refinement · Raman analysis · Magnetic and microwave properties

## 1 Introduction

The use of electronic devices employing microwave technology has been applied in a variety of technology applications. It is commonly known that in the field of communication technology, the number of electronic devices working in high-frequency range has grown rapidly in the last few

decades, for example, geo-location system, smartphone and computer with high-frequency compatibility, wave-guide technology, radio communication, and antenna application [1]. In contrary to the rapid growth of microwave technology applications, electromagnetic wave interference (EMI) phenomenon occurs when these devices operate in high-frequency range reducing their effectiveness and causing failure of the system [2, 3]. One of the solutions to overcome the barrier is to create microwave absorbing materials which able to absorb microwave in the designated frequency range [4, 5]. Morevoer, the mechanism of the microwave radiation absorption is also very beneficial for military purposes in building stealth ship and camouflaging defense equipment against radar detection. These type of materials are often referred as microwave and radar absorbing materials

✉ Ade Mulyawan
ademulyawan@batan.go.id

1 Center for Science and Technology of Advanced Materials, National Nuclear Energy Agency, Kawasan Puspiptek, Serpong, Tangerang Selatan, Banten 15314, Indonesia

2 Research and Development Center, Ministry of Defense, Puslitbang Iptekhan, Jakarta 12450, Indonesia

(MRAM). Due to the extensive demand, research on MRAM materials has become the subject of comprehensive research.

In recent years, the utilization of ferrite-type materials as MRAM candidate has increased rapidly. Previous studies have discussed the utilization of the commonly used materials for MRAM candidate such as cubic spinel ferrite [3–8] and M-type hexaferrite [9]. Different from those typical ferrite materials, the research regarding the dielectric and magnetic properties to support the application of barium monoferrite ($BaFe_2O_4$) as MRAM candidate has attracted considerable interest. Initially, $BaFe_2O_4$ is only recognized as the co-existing phase along with other metastable phases during the synthesize process of barium hexaferrite, $BaFe_{12}O_{19}$ [10]. It was recently reported that $BaFe_2O_4$ also possess several distinct characteristics such as a strong-ferromagnetic behavior with large field coercivity [2], high Curie temperature [11], and good physical stability [12]. $BaFe_2O_4$ was also mentioned to have a comparable dielectric constant along with good microwave property parameters of magnetic permeabillity and electric permittivity[11, 13, 14]. Despite the fact that it exhibited promising properties to be applied as MRAM candidate, the large field coercivity restrained the utilization of $BaFe_2O_4$ in field application due to the requirement of large switching fields [2, 11, 15].

The unit cell of orthorhombic $BaFe_2O_4$ (space group *Bb21m*) is constructed from 8 $Ba^{2+}$ ions, 16 $Fe^{3+}$ ions, and 32 $O^{2-}$ ions. The $Ba^{2+}$ ions are located in two different coordinates at 4*a* site, while the $Fe^{3+}$ ions are located in two different coordinates at 8*b* site. Previous literature discussed structural modifications to improve the magnetic and dielectric properties of $BaFe_2O_4$ are available, but it only focused on the $Ba^{2+}$ ion substitution [2, 11, 13, 15]. Despite the fact that the magnetic properties in the $BaFe_2O_4$ system are mainly governed by the super-exchange interaction between $Fe^{3+}$ ions via $O^{2-}$ ions [11], no previous literature regarding the structural modification of $Fe^{3+}$ ions has been reported. Furthermore, it was found that the structural modification by replacing $Fe^{3+}$ ions with the combination of tetravalent and divalent ions was effective to reduce the field coercivity value of hexaferrite system while maintaining relatively high magnetization [16, 17]. Therefore, as an attempt to adjust the coercivity value of $BaFe_2O_4$ and to study further the effect of the joint substitution combining tetravalent and divalent ions, we introduce the $Mn^{4+}/Ni^{2+}$ ions to replace the occupation of $Fe^{3+}$ ions in $BaFe_2O_4$ system. Since the substantial changes of the structural parameters and physical properties of the $BaFe_2O_4$ system are expected, it will be very interesting and fundamentally important to define a correlation between the substitution process to the crystal structure modification, magnetic and microwave property parameters, and microwave absorbing ability.

From this point of view, the present work examined the correlation between the ionic substitution process, crystal structure, physical traits (magnetic and microwave property parameters), and microwave absorbing ability. We adopted the composition of $Ba_{0.9}Sr_{0.1}Fe_2O_4$ obtained from our previous work as the starting composition due to its large field coercivity value and promising microwave absorbing characteristic result [2, 18]. This composition was further modified by replacing the occupation of $Fe^{3+}$ ions with the joint substitution of $Mn^{4+}$ and $Ni^{2+}$ ions, with nominal composition of $Ba_{0.9}Sr_{0.1}Fe_{(2-2x)}(Mn,Ni)_xO_4$ ($0.0 \leq x \leq 0.5$). All compositions were synthesized by using solid-state reaction method with milling technique due to its simplicity in synthesize process to obtain the desirable phase.

## 2 Materials and Methods

A series of the $Mn^{4+}/Ni^{2+}$ co-substitution barium monoferrite with the nominal composition of $Ba_{0.9}Sr_{0.1}Fe_{(2-2x)}(Mn,Ni)_xO_4$ ($0.0 \leq x \leq 0.5$) were synthesized by using solid-state reaction method through milling process. All the compositional series were prepared from the stoichiometric quantities of barium carbonate ($BaCO_3$), strontium carbonate ($SrCO_3$), iron oxide ($Fe_2O_3$), manganese oxide ($MnO_2$), and nickel oxide (NiO) from Sigma Aldrich with purity over than 99.5%. The milling process was performed using hardened-steel vial and assisted by hardened-steel balls with ball-to-powder weight ratio 4:1; it was immersed in ethanol and constantly mixed at basic rotation speed of 1000 rpm for 5 h. The as-milled samples were dried in the oven to evaporate the ethanol and sintered in air atmosphere at 900 °C for 5 h using Advantec KL-600 furnace; it was grinded by using Agate mortar until fine powder was formed. We denote our samples as BSF, BSFMN-01, BSFMN-03, and BSFMN-05; the alphabet corresponds to the first letter of the metal elements included in the sample (Ba, Sr, Fe, Mn, and Ni) and the number indicates the amount of $Mn^{4+}/Ni^{2+}$ substitution ($x = 0.1$, 0.3, and 0.5).

The phase formation of the $Ba_{0.9}Sr_{0.1}Fe_{(2-2x)}(Mn,Ni)_xO_4$ series was identified by X-ray diffractometer PANalytical Philips in the $2\theta$ range of 10–80°, with step scan 0.0263° per second (Cu Kα radiation, $\lambda = 0.15406$ nm). Lattice parameters and detailed structural analysis were obtained from the Rietveld refinement analysis using General Structure Analysis System (GSAS) version 1 software. The 3-dimensional (3D) crystal visualization of the atomic position, bond angles, and bond lengths were collected by using VESTA software. In order to study the lattice distortion and emphasize the phase formation due to the substitution process, Raman spectroscopy analysis was performed at room temperature by using Bruker Senterra Raman spectroscopy ($\lambda = 785$ nm) over the range of 200–1600 $cm^{-1}$. The surface morphology of all series was analyzed using scanning electron microscope (SEM, JEOL JSM 6510-LA) coupled with the energy dispersive spectroscopy (EDS); it was operated at an accelerating

voltage of 20 kV with 10,000 times magnification. The magnetic hysteresis (*M-H*) loops were measured by using vibrating sample magnetometer (VSM) Oxford with 1-T magnetization at room temperature to obtain magnetic property parameters such as saturation magnetization, remanence magnetization, and field coercivity. The detailed microwave absorbing properties such as permeability, permittivity, and reflection loss (RL) values were carried out by using vector network analysis (VNA, Advantest type R3770) in the frequency range of 9 to 12 GHz.

# 3 Results

## 3.1 Phase Formation and Structural Analysis

The X-ray diffraction profiles of $Ba_{0.9}Sr_{0.1}Fe_{(2-2x)}(Mn,Ni)_xO_4$ ($0.0 \leq x \leq 0.5$) series are depicted in Fig. 1. All the diffraction peaks were indexed by comparing the results of experimental data and the Crystallography Open Database (COD). The phase formation of $BaFe_2O_4$ refers to the COD No. 4107896. The results of the matching process revealed that the main phase of $BaFe_2O_4$ was formed in all samples. The impurity phase was observed in the composition with the $Mn^{4+}/Ni^{2+}$ substitution larger than 0.1 ($x > 0.1$). The enlarged view of the diffraction profiles in the range of $2\theta = 30$–$35°$ is shown in the right side of the Fig. 1 for the clarity of the $Mn^{4+}/Ni^{2+}$ substitution at the $Fe^{3+}$ site. It shows that the diffraction peaks that correspond to the (610) and (020) planes relatively remained on the same position with a broader intensity due to the substitution process. In addition, the impurity phase was formed in the position of $2\theta \approx 31.2°$ in both composition of BSFMN-03 ($x = 0.3$) and

BSFMN-05 ($x = 0.5$). It belongs to the $BaMnO_3$ phase with the COD No. 1524992. Due to a broadening intensity phenomenon of the diffraction peaks, we calculated the crystallite size (D) of all samples by using the Williamson-Hall (W–H) method. This method acknowledges that the broadening diffraction peak as the combination effect of strain and crystallite size [19, 20]. The equation is shown as follows:

$$\beta_{hkl}\cos\theta = \frac{K\lambda}{D_{W-H}} + 4\varepsilon \sin\theta \tag{1}$$

where $\beta_{hkl}$ is the full-width at half-maximum (FWHM) obtained from the Lorentzian fitting function of the diffraction peaks, $D_{W-H}$ is the crystallite size obtained from W–H method, $K$ is the dimensionless shape factor equals to 0.89, $\lambda$ is the wavelength of Cu-K$\alpha$ radiation ($\lambda = 0.15406$ nm), $\varepsilon$ is the coefficient related to the strain effect and lattice distortion, and $\theta$ is the diffraction angle. We plotted the W–H plots of $4\sin\theta$ (X axis) vs $\beta\cos\theta$ (Y axis) and made linear fitted line, the characteristic of W–H plots can be seen in supplementary figure of Fig. S1. The $D_{W-H}$ was extracted from the intercept with vertical axis while the strain was obtained from the slope; the results are shown in Table 1. The $D_{W-H}$ was increased from 42.00 nm (BSF) to 69.30 nm (BSFMN-01); further substitution resulted in the decrease of $D_{W-H}$ to 49.50 nm (BSFMN-03) and 55.44 nm (BSFMN-05). It can be observed that the substitution of $Mn^{4+}$ (0.53 Å) and $Ni^{2+}$ (0.69 Å) replacing $Fe^{3+}$ (0.64 Å) will also induce the lattice strain. In the samples that exhibited a single-phase formation of $BaFe_2O_4$, the lattice strain was found to increase from 1.80 to 3.00 and later changed to 2.80 and 3.20 for samples with impurity phase. The trend of the lattice strain produced in all samples was found proportional to the $D_{W-H}$ values.

The detailed structural analysis to study the effect of the $Mn^{4+}/Ni^{2+}$ substitution was carried out by Rietveld refinement using GSAS software; the result of the refinement process is shown in Fig. 2, and the extracted data are summarized in the Table 1. In Fig. 2, we can see that the refinement results possess a good and reliable match from the agreement between the calculated profiles (red line) and the experimental diffraction profiles (black diamond symbol) resulting small difference (blue line) over all the $2\theta$ range. We can assure the good quality of the refinement process also from the small number of the chi square ($\chi^2$), and the small difference between $R_{wp}$ and $R_p$ where the difference is less than 2% in all samples [21], see the top side of Table 1. According to the refinement results, we confirm that the BSF and BSFMN-01 are only crystallized into an orthorhombic structure of $BaFe_2O_4$ (space group *Bb21m*). In the single-phase compositions, the $Mn^{4+}/Ni^{2+}$ co-substitution increases the lattice parameters (*a*, *b*, and *c*) and subsequently followed by the increase of the unit cell volume and the decrease of the density. The ionic radii of the $Fe^{3+}$
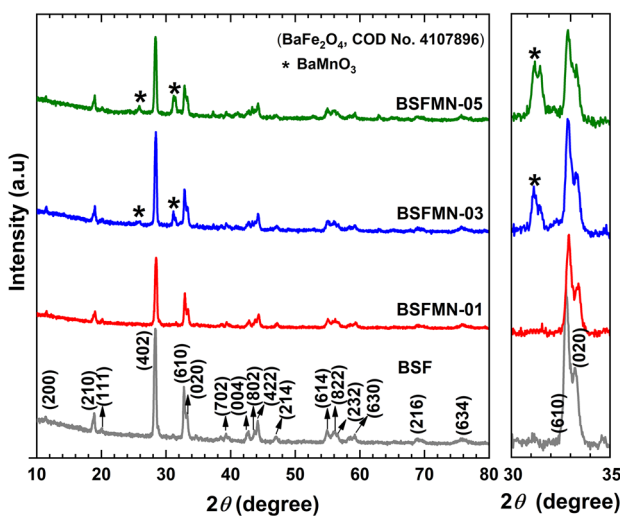


**Fig. 1** The X-ray diffraction profiles of $Ba_{0.9}Sr_{0.1}Fe_{(2-2x)}(Mn,Ni)_xO_4$ ($0.0 \leq x \leq 0.5$); the enlarge view is shown in the right side

**Table 1** The results of Williamson-Hall analysis and refined structural parameters of $Ba_{0.9}Sr_{0.1}Fe_{(2-2x)}(Mn,Ni)_xO_4$ ($0.0 \leq x \leq 0.5$) series

| Sample | BSF | BSFMN-01 | BSFMN-03 | BSFMN-05 |
|---|---|---|---|---|
| substitution ($x$) | 0 | 0.1 | 0.3 | 0.5 |
| $R_p$ (%) | 3.04 | 3.65 | 3.24 | 3.35 |
| $R_{wp}$ (%) | 3.91 | 4.60 | 4.18 | 4.35 |
| chi-square ($\chi^2$) | 1.30 | 1.15 | 1.43 | 1.62 |
| Phase 1 ($BaFe_2O_4$), *Bb21m* (orthorhombic) | | | | |
| $D_{W-H}$ (nm) | 42.00 | 69.30 | 49.50 | 55.44 |
| Strain ($\times 10^{-3}$) | 1.80 | 3.00 | 2.80 | 3.10 |
| a (Å) | 18.9523 | 18.9688 | 18.9381 | 18.9342 |
| b (Å) | 5.3748 | 5.3772 | 5.3736 | 5.3754 |
| c (Å) | 8.4576 | 8.4599 | 8.4529 | 8.4580 |
| Volume (Å$^3$) | 861.5300 | 862.8940 | 860.2100 | 866.0450 |
| Density (g cm$^{-3}$) | 5.138 | 4.742 | 4.834 | 4.830 |
| wt. ratio (%) | 100 | 100 | 95.22 | 87.14 |
| Phase 2 ($BaMnO_3$), *P63/mmc* (hexagonal) | | | | |
| a (Å) | | | 5.6939 | 5.6938 |
| b (Å) | | | 5.6939 | 5.6938 |
| c (Å) | | | 4.8208 | 4.5355 |
| Volume (Å$^3$) | | | 135.354 | 127.340 |
| Density (g cm$^{-3}$) | | | 12.637 | 13.429 |
| wt. ratio (%) | - | - | 4.78 | 12.86 |

(0.64 Å) is higher than the average of the co-substitution ionic radii, $Mn^{4+}$ (0.53 Å) and $Ni^{2+}$ (0.69 Å), so that the lattice parameters and unit cell volume are basically expected to decrease. In the contrary, the $Mn^{4+}/Ni^{2+}$ co-substitution in BSFMN-01 ($x=0.1$) led to an increase in the lattice parameters and volume. The lattice constants of the BSF sample are $a = 18.9523$ Å, $b = 5.3748$ Å, and $c = 8.4576$ Å; meanwhile in the BSFMN-01 are $a = 18.9688$ Å, $b = 5.3772$ Å, and $c = 8.4599$ Å. This phenomenon may attribute to the lattice distortion caused by the substitution process. The more detailed explanation regarding the lattice distortion and the relations with the bond length and bond distance in the system will be discussed in Sect. 4. A higher $Mn^{4+}/Ni^{2+}$ substitution ($x > 0.1$) apparently cannot be contained in the barium monoferrite cell unit and finally form the impurity phase that belongs to the anti-ferromagnetic $BaMnO_3$ phase (hexagonal, space group *P63/mmc*). The weight percentage ratio (wt. ratio) of $BaMnO_3$ in those compositions were found to be 4.78% and 12.86%, respectively. Because the presence of the anti-ferromagnetic fraction in our sample is inevitable, our study is limited to the proposed constituent compositions. In the dual-phase compositions of BSFMN-03 and BSFMN-05, the volume of unit cell and lattice parameters of $BaFe_2O_4$ were found to decrease compared to the single-phase

compositions particularly for the lattice constant of $a$. This result may arise due the aggregate formed by $BaMnO_3$ at the grain boundaries and causing lattice distortion that finally made the lattice parameter and volume to shrink. Other reason may relate to the difference of the solubility limit between the co-substitution of $Mn^{4+}$ and $Ni^{2+}$ ions owing to the difference of ionic mass and ionic radii [17, 22–24].

## 3.2 Microstructure

The microstructure and surface morphology of the samples were obtained from the scanning electron microscope (SEM) coupled with the energy dispersive spectroscopy (EDS) for the elemental analysis. The SEM images of the $Ba_{0.9}Sr_{0.1}Fe_{(2-2x)}(Mn,Ni)_xO_4$ ($0.0 \leq x \leq 0.5$) samples are shown in Fig. 3. It can be observed from the figures that the particles are roughly spherical and uniformly distributed with strong tendency for the particles to agglomerate. The average particle size of all samples was estimated from the line intercept method of the SEM images [14, 24, 25]. The particle size distribution in the BSF sample is known ranging from 200 to 650 nm with the average particle size is 560 nm. However, in the BSFMN-01 sample the particle size distribution was increased in the range size of 300 to 750 nm with the average of particle size that is 610 nm. These micrographs also showed an agreement with previous works who also mentioned the agglomeration of their $BaFe_2O_4$ nanoparticle samples [10, 15]. In the single-phase compositions, the agglomeration may arise from the long-range magnetic dipole–dipole particle interaction [26]. In the dual-phase compositions, we can observe that the particle size decreased with the higher degree of agglomeration compared to that of the single-phase compositions. The average particle size of the BSFMN-03 and BSFMN-05 was found to be 450 nm and 390 nm. The agglomeration in those samples is due to the aggregate formed by secondary particles from the smaller primary particle at the grain boundaries [27]. Especially in the BSFMN-05 sample which contained 12.86 wt.% of $BaMnO_3$, we can see the formation of a smaller secondary particle at the surface of the micrograph as marked by the red circle. In general, the average particle sizes for all samples are bigger than the crystallite size obtained from the W–H method which indicates that the particle sizes in our samples are polycrystalline. Figure 4 shows the EDS spectra of all $Ba_{0.9}Sr_{0.1}Fe_{(2-2x)}(Mn,Ni)_xO_4$ ($0.0 \leq x \leq 0.5$) samples. The spectra only show peaks belong to the element of Ba, Sr, Fe, Mn, Ni, and O with no impurity peak. The extracted data of the mass percentage and atomic percentage are summarized in Table 2. Based on the atomic percentage of the metal elements, we found the good-stoichiometric proportions of $BaFe_2O_4$ phase with an error 2–3% especially in those single-phase compositions.

**Fig. 2** Rietveld refinement of X-ray diffraction profiles of $Ba_{0.9}Sr_{0.1}Fe_{(2-2x)}(Mn,Ni)_xO_4$ series with **(a)** $x=0$, **(b)** $x=0.1$, **c** $x=0.3$, and **(d)** $x=0.5$
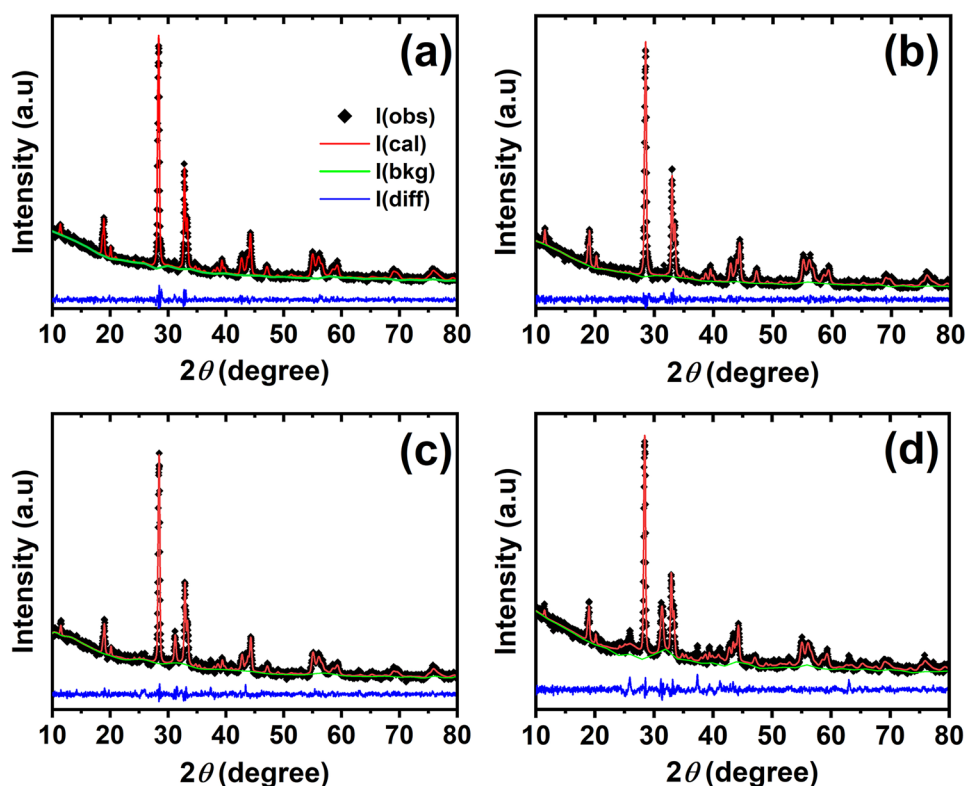


## 4 Discussion

### 4.1 3D-Crystal Visualization and Raman Analysis

In order to explain better regarding the lattice distortion in the $BaFe_2O_4$ system due to the $Mn^{4+}/Ni^{2+}$ co-substitution, the 3-dimensional (3D) crystal structure and atomic position of barium monoferrite is drawn in Fig. 5. The sketch was illustrated by using the VESTA software. The unit cell of $BaFe_2O_4$ is constructed from 8 $Ba^{2+}$ ions, 16 $Fe^{3+}$ ions, and 32 $O^{2-}$ ions. The $Ba^{2+}$ ions are located in two different coordinates ($Ba_1$ and $Ba_2$) at $4a$ site; the $Ba_1$ and $Ba_2$ are surrounded by 7 and 11 $O^{2-}$ ions, respectively. The $Fe^{3+}$ ions are also located in two different coordinates ($Fe_1$ and $Fe_2$) at $8b$ site; each $Fe^{3+}$ ion is placed in the center of four $O^{2-}$ ions to form a tetrahedral. The atomic position and polyhedral form of each ion are shown the right side of Fig. 5 for a clearer perspective of the $BaFe_2O_4$ crystal structure.

For a comparison of the ionic positions between the original and the highest substitution compositions, the refined ionic positions that belong to the BSF and BSFMN-05 compositions are shown in Tables 3, 4. From the tables, we can notice that the $Mn^{4+}/Ni^{2+}$ co-substitution affected the lattice distortion of all sites in the $BaFe_2O_4$ system. Therefore, we tried to summarize other important information such as bond lengths and bond angles in the orthorhombic system of all compositions to study further the effect of the $Mn^{4+}/Ni^{2+}$

substitution; the representative results are summarized in Table 5. Reminiscing the increasing lattice constants and cell volume of $BaFe_2O_4$ in the BSFMN-01 sample compared to the BSF sample, we can see this phenomenon is highly attributed to the lattice distortion induced by the $Mn^{4+}/Ni^{2+}$ co-substitution as evidenced from the fluctuations of the bond angles and bond lengths. The sharp increase of the bond angle ($O_4$-$Fe_1$-$O_2$) and bond lengths ($Fe_1$-$O_1$ and $Fe_2$-$O_3$) in BSFMN-01 sample are responsible for the increase of the lattice constants and cell volume relative to the BSF sample; the representative bond lengths and bond angles in BSF and BSFMN-01 are illustrated in the top side of Fig. 6. The same mechanism also happened in the dual-phase compositions of BSFMN-03 and BSFMN-05. The proportional results of the lattice constants and cell volume with the bond angles and bond lengths are resulted from the fluctuations of the $O_3$-$Fe_2$-$O_2$ angle, $Fe_2$-$O_5$ bond, and $Fe_1$-$O_1$ bond in those compositions. Another example of the lattice distortion occurring at $8b$ site between the BSF and BSFMN-03 sample was depicted in the bottom side of Fig. 6.

Raman spectroscopy is a powerful tool to study the change of the atomic structure since vibrational modes are very sensitive to detect ordering in the sample due to the atomic vibration, lattice distortion, or substitution process [28–30]. To support the results of the refinement from XRD measurement, Raman spectroscopy was carried out
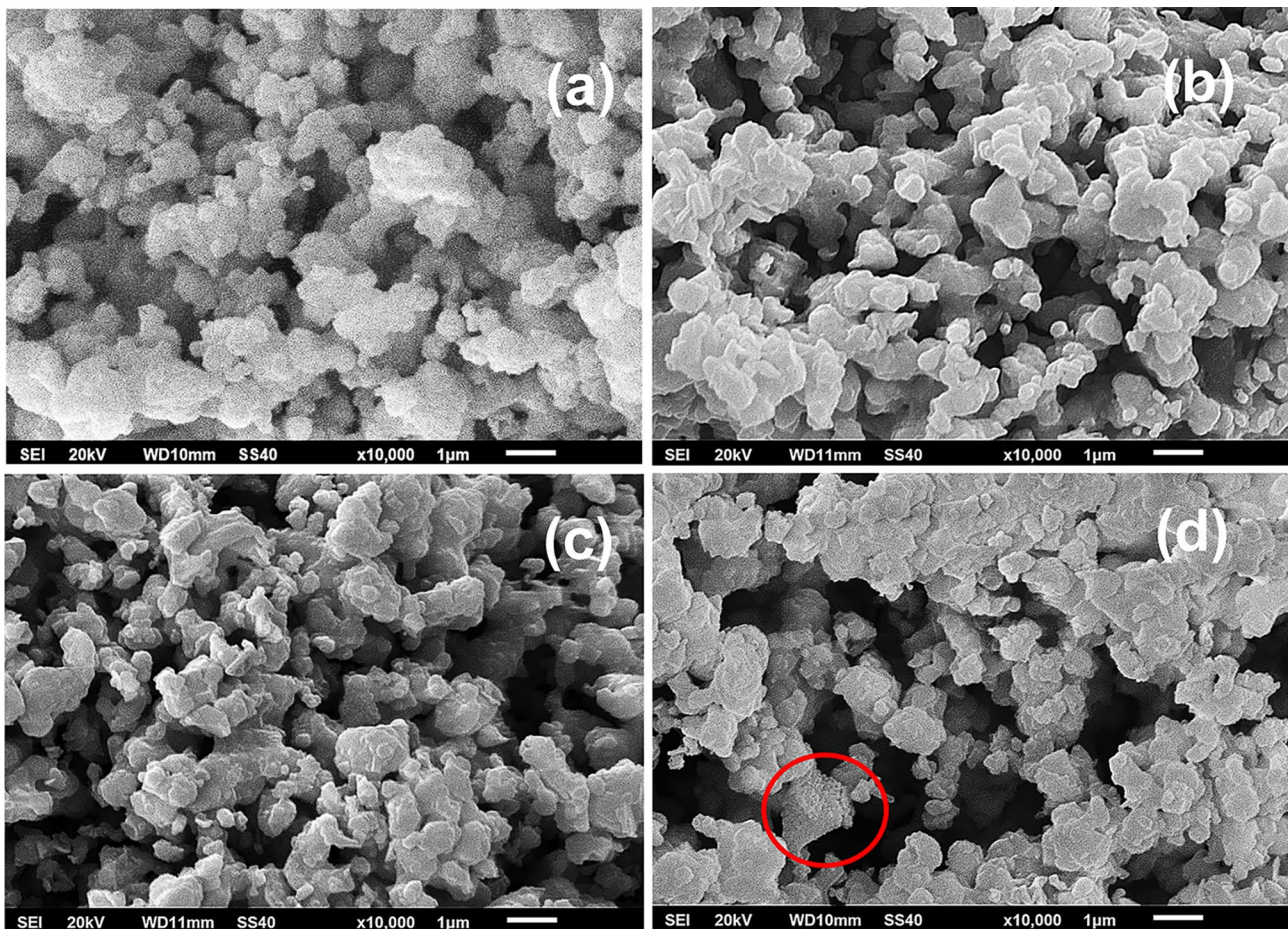
**Fig. 3** The SEM images of the $Ba_{0.9}Sr_{0.1}Fe_{(2-2x)}(Mn,Ni)_xO_4$ ($0.0 \leq x \leq 0.5$) series with **(a)** $x=0$, **(b)** $x=0.1$, **(c)** $x=0.3$, and **(d)** $x=0.5$

in the range of 200–1600 $cm^{-1}$. The Raman spectra of all $Ba_{0.9}Sr_{0.1}Fe_{(2-2x)}(Mn,Ni)_xO_4$ ($0.0 \leq x \leq 0.5$) series together with the Lorentzian fitting (blue lines) are depicted in Fig. 7. The unit cell of $BaFe_2O_4$ (space group: *Bb21m*) is consisted of 56 ions located in two different sites of 4*a* and 8*b*. According to the group theory analysis obtained from the Bilbao crystallographic server, there are 63 Raman active phonon modes at the Γ points in the orthorhombic system of $BaFe_2O_4$. The Γ corresponds to the center of the Brillouin zone. The detailed Raman active phonon modes of the system are predicted as follows:

$$\Gamma_{Raman} = 19A_1 + 13A_2 + 12B_1 + 19B_2 \qquad (2)$$

As seen in Fig. 7, the number of peaks was less than predicted from group theory analysis due to the overlapping peaks and the low intensity of Raman phonon modes [31, 32]. The lattice distortions due to the $Mn^{4+}/Ni^{2+}$ co-substitution observed by XRD measurement are now confirmed from the results of Raman spectra. In the single-phase compositions of BSF and BSFMN-01, the most prominent peak and the spectra below the range of 400 $cm^{-1}$ are slightly shifted to the

lower wavenumber with the increase of the $Mn^{4+}/Ni^{2+}$ substitution in $BaFe_2O_4$. In addition, the peaks at 573 and 600 $cm^{-1}$ joined to become one peak in the BSFMN-01 sample. The most prominent peak in BSF sample at around 450–550 $cm^{-1}$ is consisted of at least three deconvoluted Raman spectra. Referring to our previous study [2], this peak was associated to the vibration of the $Ba^{2+}$ and the stretching of the $O^{2-}$ ion in the 4*a* site of $BaFe_2O_4$. In BSFMN-01 sample, the decreasing number of deconvoluted Raman spectra in the most prominent peak shows that the 4*a* site was also affected by the $Mn^{4+}/Ni^{2+}$ substitution in the system. The changes of Raman spectra below 400 $cm^{-1}$ and at around 600 $cm^{-1}$ were associated to the stretch of phonon active modes of the tetrahedral structure as evidenced from the results of the bond lengths and bond angle in the early part of the discussion. In BSFMN-01 ($x=0.1$) and BSFMN-03 ($x=0.3$) samples, the Raman scattering formation of both compositions did not show drastic changes, but we can notice the decreasing number of the deconvoluted peak in the most prominent peak at 496 $cm^{-1}$ and the emergence of a new peak at 375 $cm^{-1}$ which associated to the formation of the $BaMnO_3$ phase. This result
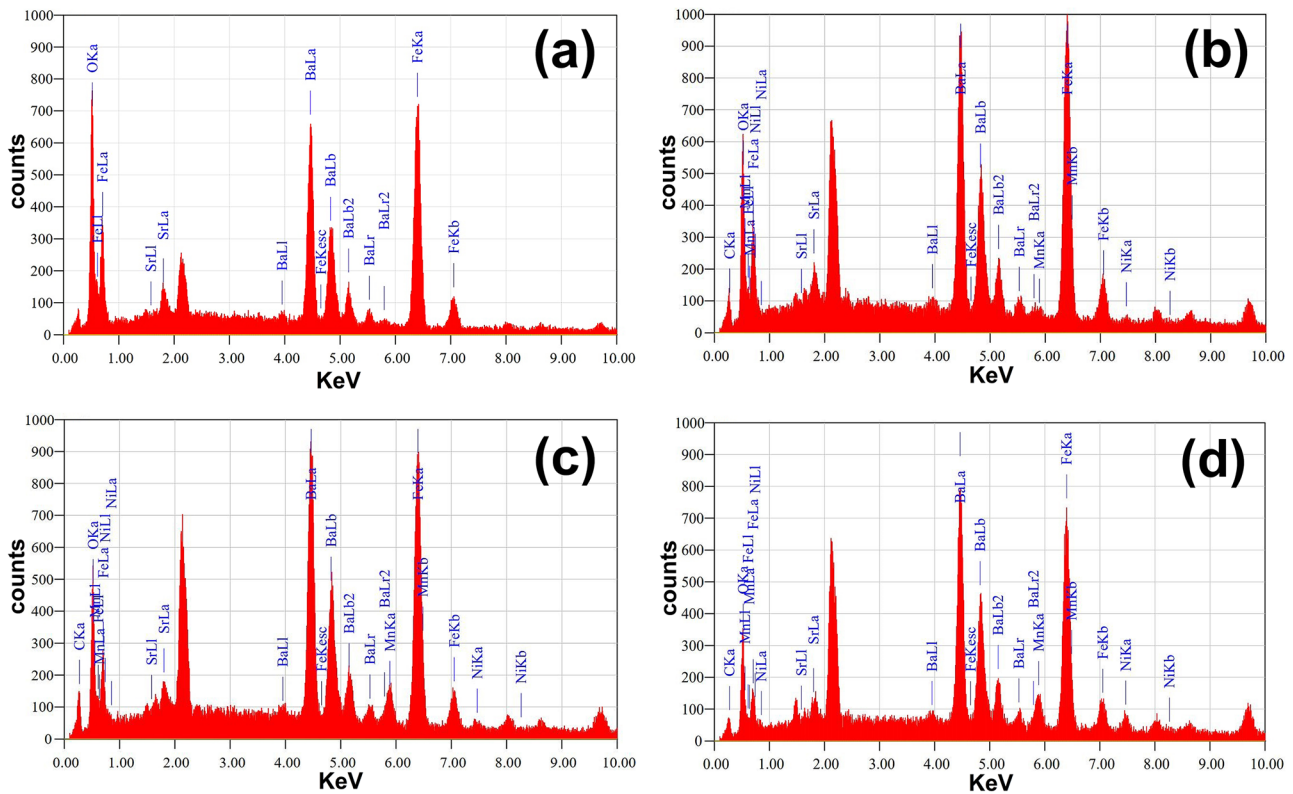
**Fig. 4** The EDS spectra of $Ba_{0.9}Sr_{0.1}Fe_{(2-2x)}(Mn,Ni)_xO_4$ ($0.0 \leq x \leq 0.5$) series with **(a)** $x=0$, **(b)** $x=0.1$, **(c)** $x=0.3$, and **(d)** $x=0.5$

showed an accordance with the refinement results where the initial impurity phase of $BaMnO_3$ was formed in the BSFMN-03 sample. As we increased the $Mn^{4+}/Ni^{2+}$ substitution in BSFMN-05 sample, the Raman spectra changed drastically since the wt.% fraction of $BaMnO_3$ phase was also increased. The Raman spectra at 375 $cm^{-1}$ became the most prominent peak along with the appearance of the new peaks at 258 and 413 $cm^{-1}$. In general, the lattice distortion due to the presence of $BaMnO_3$ phase causes the peaks associated with the $Ba^{2+}$ and $Fe^{3+}$ ions at $4a$ and $8b$ sites to change, so we hypothesize that it also affects the magnetic properties of the system.

## 4.2 Magnetic Properties

The magnetic hysteresis (*M-H*) loops of the $Ba_{0.9}Sr_{0.1}Fe_{(2-2x)}$ $(Mn,Ni)_xO_4$ ($0.0 \leq x \leq 0.5$) series are plotted in Fig. 8a. The

extracted data of saturation magnetization ($M_s$), remanence magnetization ($M_r$), and field coercivity ($H_c$) are shown in Table 6 and plotted into graphic in Fig. 8b. The *M-H* measurements for all samples were measured at ambient temperature with maximum external field ($\mu_0H$) of 1 T. The large width of the hysteresis loop in BSF sample indicates that the parent sample possesses a hard-ferromagnetic characteristic with the $H_c$ value of 3.54 kOe. The $M_s$ and $M_r$ values are found to be 0.97 A $m^2$ $kg^{-1}$ and 0.61 A $m^2$ $kg^{-1}$, respectively. The nature of the BSF sample and the values of the magnetic parameters are in accordance with the reported values of similar material [11, 15]. The increase of the $M_s$ value in BSFMN-01 sample ($M_s = 2.50$ A $m^2$ $kg^{-1}$) is consistent with the $Mn^{4+}/Ni^{2+}$ co-substitution in the $8b$ site which may be resulted from the increase of the crystallite size relative to the parent sample and also the formation of the local strain

**Table 2** Elemental mapping of $Ba_{0.9}Sr_{0.1}Fe_{(2-2x)}(Mn,Ni)_xO_4$ ($0.0 \leq x \leq 0.5$) series

| Sample | Mass (%) | | | | | | Atomic (%) | | | | | |
|---|---|---|---|---|---|---|---|---|---|---|---|---|
| | Ba | Sr | Fe | Mn | Ni | O | Ba | Sr | Fe | Mn | Ni | O |
| BSF | 41.58 | 3.17 | 36.83 | - | - | 18.42 | 14.08 | 1.68 | 30.68 | - | - | 53.55 |
| BSFMN-01 | 42.96 | 3.30 | 37.53 | 0.12 | 0.88 | 11.49 | 15.13 | 1.82 | 32.51 | 0.11 | 0.62 | 34.75 |
| BSFMN-03 | 43.46 | 2.90 | 34.17 | 3.12 | 1.14 | 10.03 | 15.10 | 1.58 | 29.19 | 2.71 | 0.92 | 29.92 |
| BSFMN-05 | 46.75 | 2.67 | 33.14 | 3.48 | 3.4 | 8.04 | 18.93 | 1.69 | 33.00 | 3.52 | 3.22 | 27.95 |

**Fig. 5** Crystal structure and ionic positions of barium mono-ferrite (BaFe$_2$O$_4$)
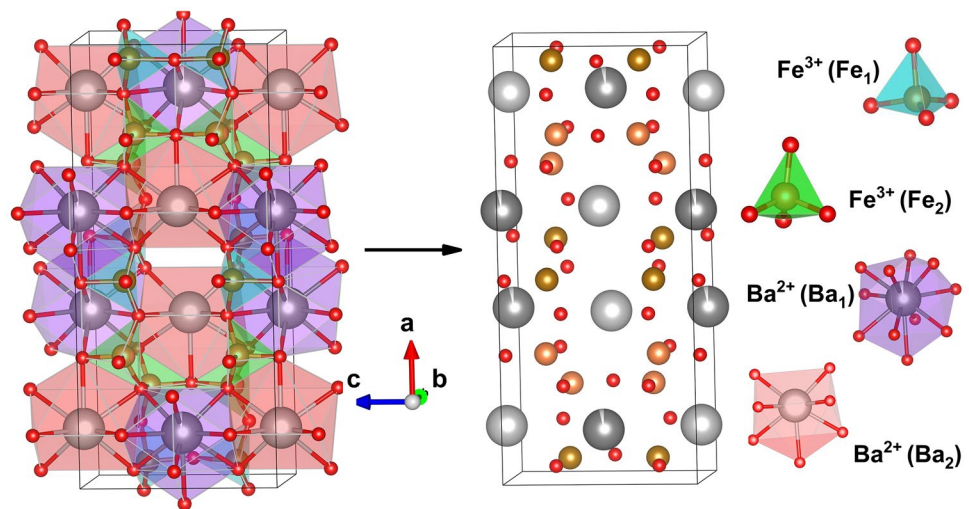


giving the re-arrangement of the FM collinearity in the system [33–37]. The decrease of the $M_s$ value was observed as we further increased the Mn$^{4+}$/Ni$^{2+}$ substitution in BSFMN-03 and BSFMN-05 samples. This result can be attributed to the excessive substitution of Mn$^{4+}$ and Ni$^{2+}$ ions to replace Fe$^{3+}$ ion in 8$b$ site that led to the formation of the impurity phase and less amount of super-exchange interaction in the system [11, 38]. It also shows a consistency with the results of the refinement process mentioning that the formation of the AFM BaMnO$_3$ was found to be 4.78 and 12.86 wt.% in BSFMN-03 and BSFMN-05 samples, respectively.

We found that the Mn$^{4+}$/Ni$^{2+}$ substitution affected the nature of the magnetic characteristic from hard to soft ferromagnetic behavior with low substitution level. In single-phase compositions, the coercivity ($H_c$) value was dropped drastically from 3.30 kOe in BSF sample to 0.65 kOe in BSFMN-01 sample. In dual-phase compositions, the $H_c$ value was decreased from 1.00 kOe and 0.70 kOe in BSFMN-03 and BSFMN-05, respectively. The Wasp-Waist formation phenomenon found in the samples is due to the exchange of the magnetic coupling interaction between two

different magnetically ordered system of ferromagnetic and anti-ferromagnetic [39, 40]. Similar phenomenon was also found in other research by Heiba et al. [15] and Dimri et al. [11]; they mentioned that this phenomenon is related to the pinning domains and magneto-crystalline anisotropy. In fact, magnetic anisotropy is also considered to be one of the important factors to determine the magnetic and microwave properties of ferromagnetic materials [17, 41–44]. Accordingly, we decided to calculate magneto-crystalline anisotropy constant ($K$) using the Stoner-Wohlfarth equation [45]:

$$H_c = \frac{2K}{\mu_0 M_s} \tag{3}$$

where $\mu_0$ is the permeability in vacuum ($4\pi \times 10^7$ H/m), $H_c$ is the field coercivity, and $M_s$ is the saturation magnetization. From the results in Table 6, we noticed that the substitution

**Table 3** Refined ionic positions of BSF ($x=0$, Ba$_{0.9}$Sr$_{0.1}$Fe$_2$O$_4$) sample

| Atom | Site | X/a | Y/b | Z/c |
|------|------|-----|-----|-----|
| Ba$_1$ | 4a | 0.127112 | 0.27154 | 0 |
| Ba$_2$ | 4a | 0.618114 | 0.2473 | 0 |
| Fe$_1$ | 8b | 0.039046 | 0.736963 | 0.274075 |
| Fe$_2$ | 8b | 0.208984 | 0.76041 | 0.289546 |
| O$_1$ | 8b | 0.03051 | 0.404273 | 0.23531 |
| O$_2$ | 8b | 0.123 | 0.917 | 0.225 |
| O$_3$ | 4a | 0.212408 | 0.407998 | 0.280604 |
| O$_4$ | 4a | 0.456109 | 0.293859 | 0 |
| O$_5$ | 4a | 0.286453 | 0.283464 | 0 |

**Table 4** Refined ionic positions of BSFMN-05 ($x=0.5$, Ba$_{0.9}$Sr$_{0.1}$Fe(Mn$_{0.5}$,Ni$_{0.5}$)O$_4$) sample

| Atom | Site | X/a | Y/b | Z/c |
|------|------|-----|-----|-----|
| **Phase 1 (BaFe$_2$O$_4$), s.g: *Bb21m* (orthorombic)** | | | | |
| Ba$_1$ | 4a | 0.130948 | 0.281959 | 0 |
| Ba$_2$ | 4a | 0.618766 | 0.250362 | 0 |
| Fe$_1$ | 8b | 0.040816 | 0.736351 | 0.28042 |
| Fe$_2$ | 8b | 0.210785 | 0.749661 | 0.286289 |
| O$_1$ | 8b | 0.024415 | 0.406808 | 0.207379 |
| O$_2$ | 8b | 0.147863 | 0.879206 | 0.222807 |
| O$_3$ | 4a | 0.205293 | 0.413406 | 0.261696 |
| O$_4$ | 4a | 0.453 | 0.226 | 0 |
| O$_5$ | 4a | 0.28 | 0.226 | 0 |
| **Phase 2 (BaMnO$_3$), s.g: *P63/mmc* (hexagonal)** | | | | |
| Ba | 2d | 0.333 | 0.667 | 0.75 |
| Mn | 2a | 0 | 0 | 0 |
| O | 6 h | 0.158 | 0.316 | 0.25 |

**Table 5** Representative data of bond lengths and bond angles at different site in $Ba_{0.9}Sr_{0.1}Fe_{(2-2x)}(Mn,Ni)_xO_4$ $(0.0 \leq x \leq 0.5)$ series

| Site | 8b | 8b-Fe$_1$ | | | 8b-Fe$_2$ | | |
|---|---|---|---|---|---|---|---|
| Angle (°) | Fe$_1$-O$_2$-Fe$_2$ | O$_2$-Fe$_1$-O$_1$ | O$_1$-Fe$_1$-O$_1$' | O$_4$-Fe$_1$-O$_2$ | O$_3$-Fe$_2$-O$_2$ | O$_3$-Fe$_2$-O$_3$' | O$_2$-Fe$_2$-O$_3$ |
| BSF | 115.15 | 122.12 | 115.65 | 95.45 | 114.80 | 113.64 | 117.19 |
| BSFMN-01 | 113.80 | 117.61 | 106.70 | 104.86 | 113.24 | 113.03 | 113.24 |
| BSFMN-03 | 119.51 | 114.06 | 105.79 | 99.88 | 112.71 | 119.52 | 112.27 |
| BSFMN-05 | 115.03 | 115.02 | 104.72 | 110.90 | 120.81 | 109.25 | 120.81 |
| Length (Å) | Fe$_1$-Fe$_2$ | Fe$_1$-O$_1$ | Fe$_1$-O$_1$' | Fe$_1$-O$_2$ | Fe$_2$-O$_2$ | Fe$_2$-O$_3$' | Fe$_2$-O$_5$ |
| BSF | 3.2258 | 1.8251 | 1.6291 | 1.9079 | 1.9136 | 1.7891 | 1.7863 |
| BSFMN-01 | 3.1375 | 1.8847 | 1.7194 | 2.0602 | 1.6766 | 1.8550 | 1.7747 |
| BSFMN-03 | 3.2270 | 1.9049 | 1.6607 | 2.2270 | 1.4839 | 1.8256 | 1.8230 |
| BSFMN-05 | 3.2183 | 2.0113 | 1.9296 | 2.1040 | 1.7027 | 1.3208 | 1.9162 |

of $Mn^{4+}/Ni^{2+}$ ions was also responsible for the change in the anisotropy field which was confirmed by a decrease in the magneto-crystalline ($K$) constant. The correlation between $K$ constant and microwave properties of the samples will be discussed in the following section.

### 4.3 Microwave Properties and Microwave Absorbing Ability

Microwave and radar absorbing materials (MRAM) are supposed to be able to absorb the electromagnetic wave in the designated frequency range by converting the energy into thermal energy [9, 43, 46]. The quality of the MRAM materials generally depends on several factors: complex permittivity ($\varepsilon_r, \varepsilon_r = \varepsilon' - j\varepsilon''$), complex permeability ($\mu_r, \mu_r = \mu' - j\mu''$), impedance matching characteristic, and microstructure [3, 4, 8]. The $\varepsilon'$ represents the real part of the complex permittivity while $\varepsilon''$ is the imaginary part of the complex permittivity. In the same manner, the $\mu'$ and $''$ represent the real and imaginary parts of the complex permeability.

The real parts of the $\varepsilon'$ and $\mu'$ are related to the ability to store electric and magnetic energy, while the imaginary parts of the $\varepsilon''$ and $\mu''$ are related to the attenuation
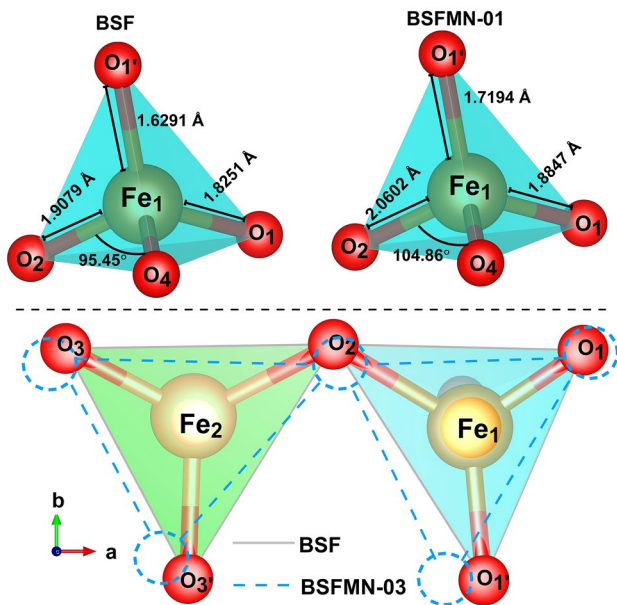
**Fig. 6** *top* Variations of bond lengths and bond angles in BSF sample ($x=0$) and BSFMN-01 ($x=0.1$) sample. *bottom* Structural distortions in BSF sample ($x=0$) compared to the BSFMN-01 ($x=0.3$) sample
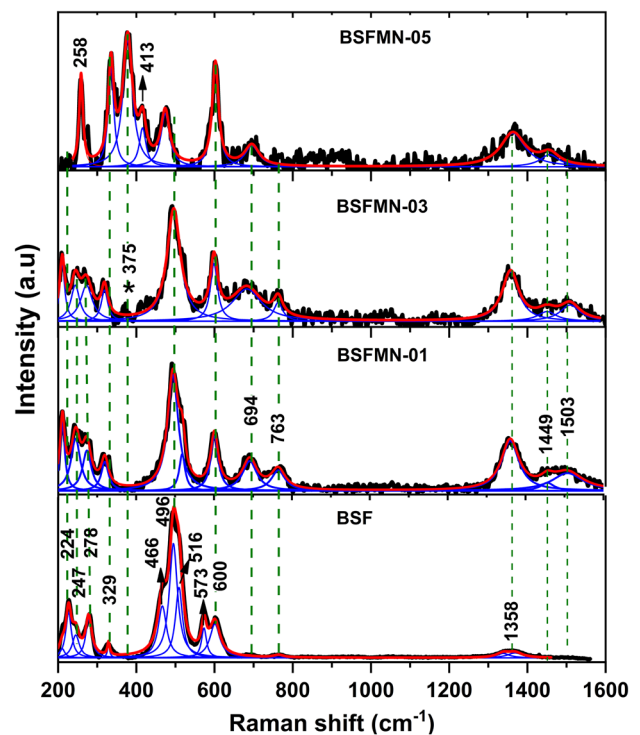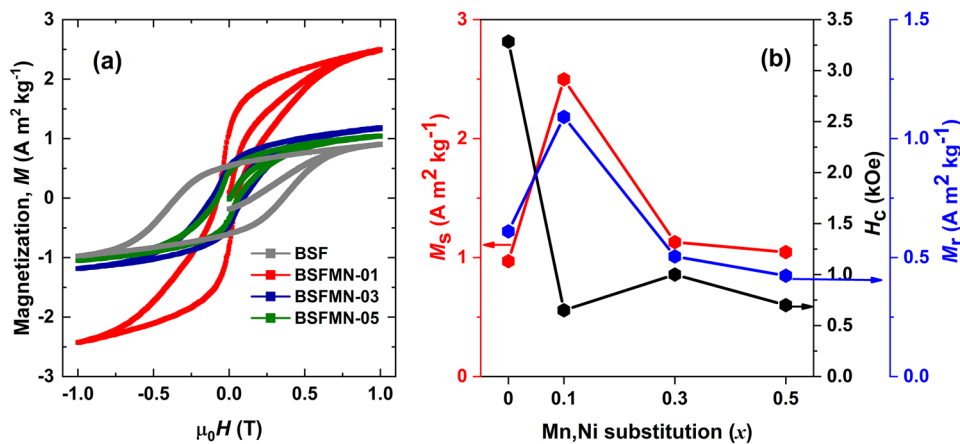
**Fig. 7** Raman spectra of $Ba_{0.9}Sr_{0.1}Fe_{(2-2x)}(Mn,Ni)_xO_4$ $(0.0 \leq x \leq 0.5)$ series together with the Lorentzian fitting (blue lines) for all samples

**Fig. 8** (a) The magnetic hysteresis (*M-H*) loops of $Ba_{0.9}Sr_{0.1}Fe_{(2-2x)}(Mn,Ni)_xO_4$ $(0.0 \le x \le 0.5)$ series; the *M-H* loop of BSF sample is from our previous work (ref. [2]). (b) Variations of the magnetic property parameters of $Ba_{0.9}Sr_{0.1}Fe_{(2-2x)}(Mn,Ni)_xO_4$ $(0.0 \le x \le 0.5)$ series



ability of the electric and magnetic energy [47]. The results of the abovementioned parameters from VNA measurement in the frequency range of 9–12 GHz for all $Ba_{0.9}Sr_{0.1}Fe_{(2-2x)}(Mn,Ni)_xO_4$ $(0.0 \le x \le 0.5)$ series are shown in Fig. 9a–d. In complex permittivity, it can be seen in Fig. 9a, b that the $\varepsilon'$ fluctuates in the range of 1.80–2.10 while the $\varepsilon''$ shows notable resonance peaks in different positions with the value between 0–0.25. Since the $\varepsilon''$ corresponds to the attenuation ability of electric energy, the formation of resonance peaks indicates the change of dielectric loss over the frequency range. Referring to the electromagnetic theory, the dielectric loss is influenced by the polarization relaxation mechanisms in the system. The relation between parameters which affected the $\varepsilon''$ is shown below:

$$\varepsilon'' = \frac{(\varepsilon_s - \varepsilon_\infty)\omega\tau}{(1 + (\omega\tau)^2)} \tag{4}$$

where $\varepsilon_s$ refers to the static dielectric constant, $\varepsilon_\infty$ is the optical frequency permittivity, $\omega$ is the angular frequency, and $\tau$ is the relaxation time. When we introduced the $Mn^{4+}/Ni^{2+}$ to replace $Fe^{3+}$ in $BaFe_2O_4$, it changed the intensity of the electron relaxation polarization in the system. In addition, particle size also affected the polarization of dipoles by changing the amount of dipole content. The effect of the

particle size to the polarization dipoles was also mentioned in other research who studied the ferrite material [23, 42, 47, 48]. Therefore, these two types of polarization factors are likely responsible to explain the relaxation mechanisms which influence the dielectric loss in the sample.

In complex permeability, we can notice in Fig. 9c, d that the $\mu'$ gradually increase until near 10 GHz then fluctuates in a relatively constant value between 0.80 and 1.10 in higher frequency range. The observed constant value of $\mu'$ is actually a common feature appearing in ferrite-type materials due to the relaxation mechanism of the magnetic dipole alignment [3, 49]. In case of $\mu''$, it fluctuates in the range of 0.20 to 0.60 with different peak positions of magnetic loss over the frequency range of 9–12 GHz. Several factors related to the magnetic effect are considered to be responsible for the magnetic loss: hysteresis loss, eddy-current loss, and magnetic resonance loss. Hysteresis loss might contribute to the magnetic loss considering to the drastic changes of the magnetic parameters due to the substitution process such as field coercivity, magneto-crystalline anisotropy constant, and saturation magnetization as we mentioned in Sect. 4. In order to confirm the contribution of the eddy-current loss in magnetic loss, we performed the calculation of $C_0$ constant using the Maxwell equation as follows:

$$C_0 = f^{-1}(\mu')^{-2}\mu'' = \frac{2}{3}\pi\mu_0 d^2\sigma \tag{5}$$

where $\mu_0$ is the permeability in vacuum ($4\pi \times 10^7$ H/m), $\sigma$ is the electric conductivity, and $d$ is the size of the material. Based on Eq. 5, we can notice that the $C_0$ is a constant related to the electric conductivity and size of the material but independent of the frequency. By thus, if eddy-current loss is the main cause of the magnetic loss, the $C_0$ constant must form a straight line with a constant value throughout the frequency range. Figure 10 shows the results of $C_0$ constant as the function of frequency. Apparently, the $C_0$ constant value of every sample decreased drastically in lower frequency range then fluctuated in the frequency range of

**Table 6** Saturation magnetization ($M_s$), remanence magnetization ($M_r$), field coercivity ($H_c$), and magneto-crystalline anisotropy constant ($K$) of $Ba_{0.9}Sr_{0.1}Fe_{(2-2x)}(Mn,Ni)_xO_4$ $(0.0 \le x \le 0.5)$ series. The experimental data of BSF sample are from our previous work (ref. [2])

| Sample | BSF | BSFMN-01 | BSFMN-03 | BSFMN-05 |
|---|---|---|---|---|
| Mn,Ni substitution (x) | 0 | 0.1 | 0.3 | 0.5 |
| $M_s$ (A m² kg⁻¹) | 0.97 | 2.50 | 1.13 | 1.05 |
| $M_r$ (A m² kg⁻¹) | 0.61 | 1.09 | 0.51 | 0.42 |
| $H_c$ (kOe) | 3.30 | 0.65 | 1.00 | 0.70 |
| $K$ (H A² kg⁻¹) | 0.16 | 0.08 | 0.06 | 0.04 |

**Fig. 9** Frequency dependence of the permittivity and permeability complex parameters of (**a**) $\varepsilon'$, (**b**) $\varepsilon''$, (**c**) $\mu'$, and (**d**) $\mu''$
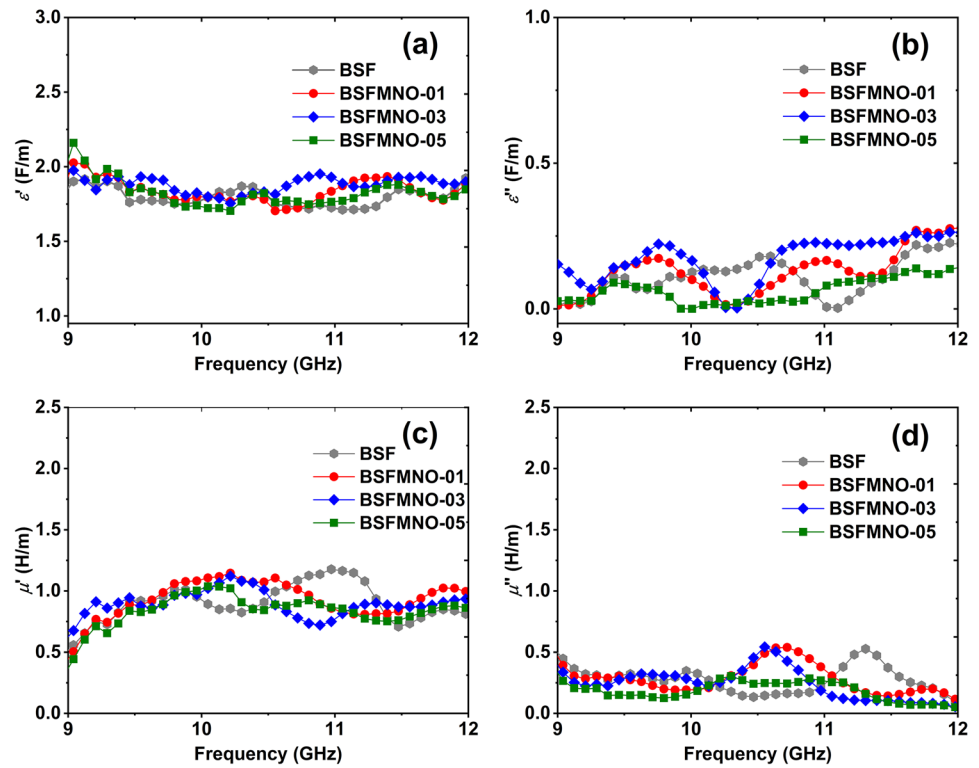


9.5–12 GHz. The results confirmed that the eddy current was not the main contribution of magnetic loss in this frequency range. The fluctuation of the $C_0$ constant value also gave us the hint that the magnetic loss was due to the magnetic resonance loss, which originated from the natural ferromagnetic resonance. According to Almessiere et al., the natural ferromagnetic resonance arises from the peculiarities of the magnetic structure due to the ordering of $Fe^{3+}$ ion, the change of Fe–O bond length, and local anion environment [33]. Those indications fitted really well with our work as we found that the $Mn^{4+}/Ni^{2+}$ co-substitution has been proven to change the Fe–O bond lengths and bond angles and also induced the charge ordering of $Fe^{3+}$ ions in $BaFe_2O_4$ system. Consequently, it can be inferred that the hysteresis loss and magnetic resonance loss originated from natural ferromagnetic resonance are the main contribution of the magnetic loss. Since the $\varepsilon''$ and $\mu''$ values directly reflect the attenuation ability of the material and it showed different peak positions in the frequency range of 9–12 GHz, distinct characteristic and microwave absorbing ability due to the substitution process are expected.

The ability of materials to attenuate microwave is commonly determined by measuring the reflection loss (RL) in the designated frequency. In this work, the RL measurement was measured by Advantest type R3770 at ambient temperature and in the frequency range of 9–12 GHz. The RL calculation of materials was carried out using the following equation:

$$RL(dB) = 20\log\left|\frac{Z_{in} - 1}{Z_{in} + 1}\right| \tag{6}$$

where $Z_{in}$ is the normalized input impedance. The detailed definition of $Z_{in}$ is given by

$$Z_{in} = \sqrt{\frac{\mu_r}{\varepsilon_r}}\tanh\left[j\frac{2\pi f d}{c}\sqrt{\mu_r \varepsilon_r}\right] \tag{7}$$
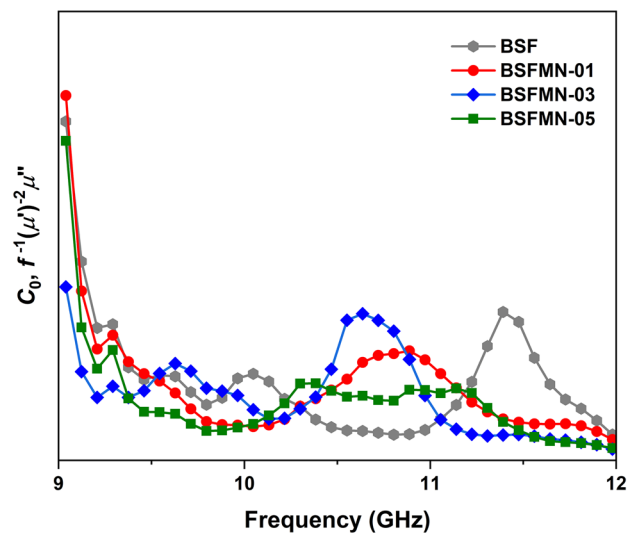


**Fig. 10** Frequency dependence of the $C_0$ constant of $Ba_{0.9}Sr_{0.1}Fe_{(2-2x)}(Mn,Ni)_xO_4$ ($0.0 \leq x \leq 0.5$) series

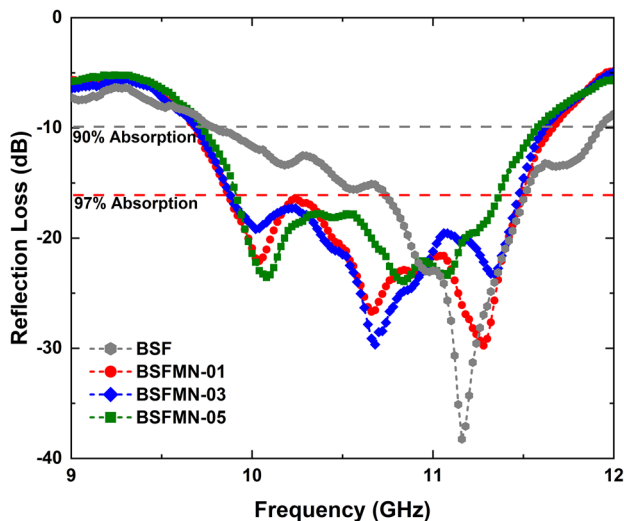**Fig. 11** Microwave absorbing ability of all $Ba_{0.9}Sr_{0.1}Fe_{(2-2x)}(Mn,Ni)_xO_4$ ($0.0 \leq x \leq 0.5$) series in the frequency range of 9–12 GHz. The RL curve of BSF sample is from our previous work (ref. [2])

where $c$ is the speed of light in vacuum and $j$ is the imaginary unit. From Eq. 7, it can be seen that $Z_{in}$ and RL values depend on to the complex permeability ($\mu_r$), complex permittivity ($\varepsilon_r$), frequency of the microwave ($f$), and thickness of the sample ($d = 2$ mm). It should be noted that the MRAM materials supposed to have minimum RL value with wide bandwidth of frequency range. In field application, materials which possess of at least RL $= -10$ dB (equals to 90% attenuation of the incident microwave energy) can be considered as effective MRAM materials [8].

The microwave attenuation for all $Ba_{0.9}Sr_{0.1}Fe_{(2-2x)}(Mn,Ni)_xO_4$ ($0.0 \leq x \leq 0.5$) series in the frequency range of 9–12 GHz are depicted in Fig. 11; the extracted data are summarized in Table 7. The BSF sample ($x = 0$) exhibited a characteristic sharp RL curve with single attenuation peak. The effective RL bandwidth (RL $< -10$ dB) was 2.12 GHz, and the minimum RL value reached $-38.25$ dB ($\approx 99.98\%$ attenuation) at 11.16 GHz. In the substituted samples, the minimum RL value was shifted to lower frequency

with lower RL values. The minimum RL values of each BSFMN-01, BSFMN-03, and BSFMN-05 are $-29.76$ dB (11.28 GHz), $-29.67$ dB (10.68 GHz), and $-23.58$ dB (10.08 GHz), which, respectively, are equivalent to 99.89%, 99.88%, and 99.56% microwave attenuation. Eventhough the depth of the RL curves in substituted samples was found lower compared to the original BSF sample, we can clearly see that the $Mn^{4+}/Ni^{2+}$ co-substitution made the RL curves remained broad at higher attenuation level. In the same Fig. 11, the RL bandwidth in BSF sample was changed drastically. At the effective RL bandwidth equals to 97% of microwave attenuation (RL $< -16.5$ dB) as marked by the red-dashed line, the bandwidth decreased 35% to 0.76 GHz. In the BSFMN-01 sample, the effective RL bandwidth (RL $< -10$ dB) equals to 90% was 2.00 GHz and the RL bandwidth (RL $< -16.5$ dB) was decreased only 17.5% to 1.65 GHz. Surprisingly, the BSFMN-03 that contains 4.78 wt.% $BaMnO_3$ phase still showed a relatively same characteristic RL curve; the RL bandwidth (RL $< -16.5$ dB) was only decrease 16% to 1.60 GHz. The weakening effect due to the excessive $Mn^{4+}/Ni^{2+}$ substitution become obvious in BSFMN-05; the 12.86 wt.% of $BaMnO_3$ phase apparently decreased the magnetic loss and microwave absorbing ability of the sample with the RL bandwidth (RL $< -16.5$ dB) was 1.44 GHz.

The magnetic resonance loss due to the natural ferromagnetic resonance played important role in tuning the characteristic RL curve of the substituted samples to have a remaining broad bandwidth at higher attenuation level (RL $< -16.5$ dB); the natural ferromagnetic resonance phenomenon in the system is originated from the charge ordering $Fe^{3+}$ ion, the change of bond lengths, and bond angles between Fe–O in $BaFe_2O_4$ system as we mentioned in the magnetic loss discussion section. The shift of the minimum RL value to lower frequency with the increase of the $Mn^{4+}/Ni^{2+}$ substitution in $BaFe_2O_4$ system was probably attributed to the hysteresis loss due to the change in field coercivity and saturation magnetization which caused the decrease of the magneto-crystalline anisotropy constant ($K$), see the number of these parameters in Table 6. According to the Larmor equation, the relation between frequency and anisotropy field is given by

**Table 7** Important parameters reflecting the microwave absorbing ability of $Ba_{0.9}Sr_{0.1}Fe_{(2-2x)}(Mn,Ni)_xO_4$ ($0.0 \leq x \leq 0.5$) series. The experimental data of BSF sample are from our previous work (ref. [2])

| Sample | RL min (dB) | $f$ RL (GHz) | Bandwidth RL $< -10$ dB | Bandwidth RL $< -16.5$ dB |
|---|---|---|---|---|
| BSF | $-38.25$ | 11.16 | 2.12 | 0.76 |
| BSFMN-01 | $-29.76$ | 11.28 | 2.00 | 1.65 |
| BSFMN-03 | $-29.67$ | 10.68 | 1.92 | 1.60 |
| BSFMN-05 | $-23.58$ | 10.08 | 1.82 | 1.44 |

$$f_r = \frac{\gamma H_a}{2\pi} \tag{8}$$

where $f_r$ is the resonance frequency, $\gamma$ refers to the gyromagnetic ratio, and $H_a$ is the anisotropic field obtained from the equation of $H_a = 2K/Ms$ [50]. As we mentioned earlier in the Sect. 4, the substitution of the $Mn^{4+}/Ni^{2+}$ changed the characteristic of the materials from hard to soft ferromagnetic behavior owing to the re-arrangement of the ferromagnetic collinearity in the system which made the value of the field coercivity ($H_c$) decreased sharply. Since the $H_c$ proportionally correspond to the anisotropic field ($H_a$) following the Stoner-Wohlfarth equation (Eq. 3), the decrease of the $H_c$ due to the substitution process will decrease the $H_a$. By thus, the decrease of the $H_a$ subsequently shifted the resonance frequency ($f_r$) to lower frequency due to the linear relation between $H_a$ and $f_r$ as shown in Eq. 8. This results showed an agreement with previous work who mentioned the same phenomenon in hexaferrite system [9, 51]. Thus, in this current work we can generally infer that the shift of the minimum RL value is due to the hyteresis loss related to the magneto-crystalline anisotropy constant.

## 5 Conclusions

The $Mn^{4+}/Ni^{2+}$ co-substitution barium monoferrite with the nominal composition of $Ba_{0.9}Sr_{0.1}Fe_{(2-2x)}(Mn,Ni)_xO_4$ $(0.0 \leq x \leq 0.5)$ have been successfully synthesized by using solid-state reaction method with milling technique. Structural analysis based on the Rietveld refinement process in complementary with Raman analysis was studied. We found the phase formation and the fluctuation of bond angles and bond lengths due to the substitution process in all samples closely matched the phonon mode of the deconvoluted Raman spectra. We also demonstrated the correlation between the effect of the substitution process relative to the lattice distortion, magnetic properties, and microwave properties of the sample. Our results indicate that the substitution of $Mn^{4+}/Ni^{2+}$ ions is responsible not only to the sharp decrease of the field coercivity but also for the change in the anisotropy field which is confirmed by the decrease in the magneto-crystalline constant ($K$).

Microwave properties and microwave absorbing ability of all compositional series were investigated in the frequency range of 9–12 GHz. It was noticed that the $Mn^{4+}/Ni^{2+}$ co-substitution induced a reduction in the minimum RL value, but the substitution process made the RL curves remained broad at higher attenuation level (RL < − 16.5 dB, ≈ 97% microwave attenuation) compared to the parent composition. The broad feature of the RL curve with multiple attenuation peaks are associated with the magnetic resonance loss and hysteresis loss, which originated from to the natural ferromagnetic resonance due to the peculiarity of the charge ordering $Fe^{3+}$ ions and the fluctuation of bond lengths and bond angles in the substituted system. The shift in the minimum RL value to a lower frequency with an increase in $Mn^{4+}/Ni^{2+}$ ions is also associated with a decrease in the $K$ value; we find this result in accordance with the Larmor equation. It is confirmed that characteristic feature of the RL curves of barium monoferrite can also be controlled by adjusting the occupation $Fe^{3+}$ ions in the system. If this progress continues apace, we can expect a promising prospect for the application of barium monoferrite as high-frequency materials or radar absorbing material in particular.

**Author Contribution** Ade Mulyawan: conceptualization, investigation, validation, formal analysis, visualization, writing—original draft, writing—review and editing; Salim Mustofa: validation; Deswita: investigation; Raden Andhika Ajiesastra: investigation; Wisnu Ari Adi: validation, supervision, writing—review and editing.

## References

1. Houbi, A., Aldashevich, Z.A., Atassi, Y., BagasharovaTelmanovna, Z., Saule, M., Kubanych, K.: Microwave absorbing properties of ferrites and their composites: a review. J. Magn. Magn. Mater. **529**, 167839 (2021). https://doi.org/10.1016/j.jmmm.2021.167839

2. Mulyawan, A., Adi, W.A., Yunasfi, Y.: Raman spectroscopy study, magnetic and microwave absorbing properties of modified barium strontium monoferrite Ba (1-x) Sr (x) Fe2O4. Mal. J. Fund. Appl. Sci. **14** (2018). https://doi.org/10.11113/mjfas.v14n1.750

3. Yunasfi, Y., Mashadi, M., Mulyawan, A., Adi, W.A.: Synthesis of NiLaxFe(2–x)O4 system as microwave absorber materials by milling technique. J. Electron. Mater. **49**, 7272–7278 (2020). https://doi.org/10.1007/s11664-020-08489-w

4. Ari Adi, W., Yunasfi, Y.: Magnetic properties and microwave absorption characteristic of MWNT filled with magnetite coated iron nanoparticles. Mater. Sci. Eng. B Solid-State Mater. Adv. Technol. **262**, 114760 (2020). https://doi.org/10.1016/j.mseb.2020.114760

5. Yunasfi, Y., Mashadi, M., Mulyawan, A.: Magnetic and microwave absorption properties of neodymium doped nickel ferrite using milling technique. J. Teknol. **81**, 21–25 (2019). https://doi.org/10.11113/jt.v81.11045

6. Mashadi, M., Yunasfi, Y., Mulyawan, A.: Microwave absorption study of manganese ferrite in x-band range prepared by solid state reaction method. J. Teknol. **80**, 147–151 (2018). https://doi.org/10.11113/jt.v80.10773

7. Yunasfi, Y., Mulyawan, A., Mashadi, M., Suyanti, W.A.A.: Synthesis of NiCexFe(2-x)O4 (0 ≤ x ≤ 0.05) as microwave absorbing materials via solid-state reaction method. J. Magn. Magn. Mater. **532**, (2021). https://doi.org/10.1016/j.jmmm.2021.167985

8. Adi, W.A, Yunasfi, Y., Mashadi, M., Winatapura, D.S, Mulyawan, A., Sarwanto, Y., Gunanto, Y.E.Y.T.: Metamaterial: smart magnetic material for microwave absorbing material. In: Intech Open. pp. 1–18. Intech Open (2019)

9. Nikmanesh, H., Hoghoghifard, S., Hadi-Sichani, B.: Study of the structural, magnetic, and microwave absorption properties of the simultaneous substitution of several cations in the barium hexaferrite structure. J. Alloys Compd. **775**, 1101–1108 (2019). https://doi.org/10.1016/j.jallcom.2018.10.051

10. Candeia, R.A., Souza, M.A.F., Bernardi, M.I.B., Maestrelli, S.C., Santos, I.M.G., Souza, A.G., Longo, E.: Monoferrite BaFe2O4 applied as ceramic pigment. Ceram. Int. **33**, 521–525 (2007). https://doi.org/10.1016/j.ceramint.2005.10.018

11. Dimri, M.C., Khanduri, H., Agarwal, P., Pahapill, J., Stern, R.: Structural, magnetic, microwave permittivity and permeability studies of barium monoferrite (BaFe2O4). J. Magn. Magn. Mater. **486**, 165278 (2019). https://doi.org/10.1016/j.jmmm.2019.165278

12. Vijayaraghavan, T., Suriyaraj, S.P., Selvakumar, R., Venkateswaran, R., Ashok, A.: Rapid and efficient visible light photocatalytic dye degradation using AFe2O4 (A = Ba, Ca and Sr) complex oxides. Mater. Sci. Eng. B Solid-State Mater. Adv. Technol. **210**, 43–50 (2016). https://doi.org/10.1016/j.mseb.2016.04.005

13. Ahilandeswari, E., Rajesh Kanna, R., Sakthipandi, K.: Synthesis of neodymium-doped barium nanoferrite: analysis of structural, optical, morphological, and magnetic properties. Phys. B Condens. Matter. **599**, 412425 (2020). https://doi.org/10.1016/j.physb.2020.412425

14. Ahmad, M., Shaheen, J., Hashmi, W.A., Akhtar, M.N., Asif, M.: Structural, magnetic and high frequency (1–6 GHz) parameters of Sr-substituted BaFe2O4 monoferrites synthesized by sol-gel method. Mod. Phys. Lett. B. **33**, 1–16 (2019). https://doi.org/10.1142/S0217984919502191

15. Heiba, Z.K., Wahba, A.M., Mohamed, M.B.: Phase analysis and cation distribution correlated with magnetic properties of spinel Ba1−xSrxFe2O4 ferrites prepared at different annealing temperatures. J. Mater. Sci. Mater. Electron. **31**, 12482–12492 (2020). https://doi.org/10.1007/s10854-020-03795-9

16. Alsmadi, A.M., Bsoul, I., Mahmood, S.H., Alnawashi, G., Al-Dweri, F.M., Maswadeh, Y., Welp, U.: Magnetic study of M-type Ru-Ti doped strontium hexaferrite nanocrystalline particles. J. Alloys Compd. **648**, 419–427 (2015). https://doi.org/10.1016/j.jallcom.2015.06.274

17. Tanwar, K., Gyan, D.S., Gupta, P., Pandey, S., Omparkash, Kumar, D.: Investigation of crystal structure, microstructure and low temperature magnetic behavior of Ce4+ and Zn2+ co-doped barium hexaferrites (BaFe12O19). RSC Adv. **8**, 19600–19609 (2018). https://doi.org/10.1039/c8ra02455c

18. Ade Mulyawan; WA Adi; Salim Mustofa; Adel Fisli: The phase transformation and crystal structure studies of strontium substituted barium monoferrite. In: IOP Conf. Ser.: Earth Environ. Sci. p. 012070 (2017)

19. Manjunatha, K., Angadi, V.J., Oliveira, M.C., de Lazaro, S.R., Longo, E., Ribeiro, R.A.P., Manjunatha, S.O., Ayachit, N.H.: Towards shape-oriented Bi-doped CoCr2O4 nanoparticles from theoretical and experimental perspectives: structural, morphological, optical, electrical and magnetic properties. J. Mater. Chem. C. **9**, 6452–6469 (2021). https://doi.org/10.1039/d1tc00872b

20. Felhi, R., Omrani, H., Koubaa, M., Koubaa, W.C., Cheikhrouhou, A.: Enhancement of magnetocaloric effect around room temperature in Zn0.7Ni0.3-xCuxFe2O4 (0 ≤ x ≤ 0.2) spinel ferrites. J. Alloys Compd. **758**, 237–246 (2018). https://doi.org/10.1016/j.jallcom.2018.05.078

21. Toby, B.H.: EXPGUI, a graphical user interface for GSAS. J. Appl. Crystallogr. **34**, 210–213 (2001). https://doi.org/10.1107/S0021889801002242

22. Thakur, P., Sharma, R., Kumar, M., Katyal, S.C., Negi, N.S., Thakur, N., Sharma, V., Sharma, P.: Super paramagnetic la doped Mn-Zn nano ferrites: dependence on dopant content and crystallite size. Mater. Res. Express. **3**, 1–14 (2016). https://doi.org/10.1088/2053-1591/3/7/075001

23. Almessiere, M.A., Slimani, Y., Korkmaz, A.D., Baykal, A., Güngüneş, H., Sözeri, H., Shirsath, S.E., Güner, S., Akhtar, S., Manikandan, A.: Impact of La3+ and Y3+ ion substitutions on structural, magnetic and microwave properties of Ni0.3Cu0.3Zn0.4Fe2O4 nanospinel ferrites synthesized: via sonochemical route. RSC Adv. **9**, 30671–30684 (2019). https://doi.org/10.1039/c9ra06353f

24. Mustafa, G., Islam, M.U., Zhang, W., Anwar, A.W., Jamil, Y., Murtaza, G., Ali, I., Hussain, M., Ali, A., Ahmad, M.: Influence of the divalent and trivalent ions substitution on the structural and magnetic properties of Mg0.5-xCdxCo0.5Cr0.04TbyFe1.96-yO4 ferrites prepared by sol-gel method. J. Magn. Magn. Mater. **387**, 147–154 (2015). https://doi.org/10.1016/j.jmmm.2015.03.091

25. Reddy, M.V., Jayaraman, T.V., Patil, N., Das, D.: Giant magnetoelastic properties in Ce-substituted and magnetic field processed cobalt ferrite. J. Alloys Compd. **837**, 155501 (2020). https://doi.org/10.1016/j.jallcom.2020.155501

26. Peña-Garcia, R., Guerra, Y., Santos, F.E.P., Almeida, L.C., Padrón-Hernández, E.: Structural and magnetic properties of Ni-doped yttrium iron garnet nanopowders. J. Magn. Magn. Mater. **492**, 165650 (2019). https://doi.org/10.1016/j.jmmm.2019.165650

27. Almessiere, M.A., Slimani, Y., Baykal, A.: Impact of Nd-Zn co-substitution on microstructure and magnetic properties of SrFe12O19 nanohexaferrite. Ceram. Int. **45**, 963–969 (2019). https://doi.org/10.1016/j.ceramint.2018.09.272

28. Thakur, P., Sharma, R., Madolappa, S., Kundu, S.: Changes on magnetic, dielectric, electrical, impedance and modulus spectroscopic characteristics of CoFe2O4 nanoparticles synthesized by honey mediated sol-gel combustion method.

29. H'Mŏk, H.L., Martínez Aguilar, E., AntúnezGarcía, J., RibasAriño, J., Mestres, L., Alemany, P., Galván, D.H., Siqueiros Beltrones, J.M., Raymond Herrera, O.: Theoretical justification of stable ferromagnetism in ferroelectric BiFeO3 by first-principles. Comput. Mater. Sci. **164**, 66–73 (2019). https://doi.org/10.1016/j.commatsci.2019.03.040

30. Cristina De Oliveira, R., Pontes Ribeiro, R.A., Cruvinel, G.H., Ciola Amoresi, R.A., Carvalho, M.H., Aparecido De Oliveira, A.J., Carvalho De Oliveira, M., Ricardo De Lazaro, S., Fernando Da Silva, L., Catto, A.C., Simões, A.Z., Sambrano, J.R., Longo, E.: Role of surfaces in the magnetic and ozone gas-sensing properties of ZnFe2O4 nanoparticles: theoretical and experimental insights. ACS Appl. Mater. Interfaces. **13**, 4605–4617 (2021). https://doi.org/10.1021/acsami.0c15681

31. Prasetyo, A., Mihailova, B., Suendo, V., Nugroho, A.A.: Ismunandar: The effect of the A-site cation on the structural transformations in ABi4Ti4O15 (A= Ba, Sr): Raman scattering studies. J. Solid State Chem. **283**, 121131 (2020). https://doi.org/10.1016/j.jssc.2019.121131

32. Prasetyo, A., Mihailova, B., Suendo, V., Nugroho, A.A., Zulhadjri, Ismunandar: Structural transformations in Pb1 − xBi4 + xTi4 − xMnxO15 (x = 0.2 and 0.4): a Raman scattering study. J. Raman Spectrosc. **48**, 292–297 (2017). https://doi.org/10.1002/jrs.5030

33. Almessiere, M.A., Slimani, Y., Güngüneş, H., Kostishyn, V.G., Trukhanov, S.V., Trukhanov, A.V., Baykal, A.: Impact of Eu3+ ion substitution on structural, magnetic and microwave traits of Ni–Cu–Zn spinel ferrites. Ceram. Int. **46**, 11124–11131 (2020). https://doi.org/10.1016/j.ceramint.2020.01.132

34. Iqbal, M.J., Ashiq, M.N., Gomez, P.H.: Effect of doping of Zr-Zn binary mixtures on structural, electrical and magnetic properties of Sr-hexaferrite nanoparticles. J. Alloys Compd. **478**, 736–740 (2009). https://doi.org/10.1016/j.jallcom.2008.11.136

35. Warhate, V.V., Badwaik, D.S.: Structural, magnetic and thermo-magnetic properties of NiMn Y-type strontium nano-hexaferrites. J. Alloys Compd. **818**, 152830 (2020). https://doi.org/10.1016/j.jallcom.2019.152830

36. Manjunatha, K., Jagadeesha Angadi, V., Ribeiro, R.A.P., Longo, E., Oliveira, M.C., Bomio, M.R.D., de Lázaro, S.R., Matteppanavar, S., Rayaprol, S., Babu, P.D., Pasha, M.: Structural, electronic, vibrational and magnetic properties of Zn2+ substituted MnCr2O4 nanoparticles. J. Magn. Magn. Mater. **502**, 166595 (2020). https://doi.org/10.1016/j.jmmm.2020.166595

37. Manjunatha, K., Angadi, V.J., Ribeiro, R.A.P., Oliveira, M.C., De Lázaro, S.R., Bomio, M.R.D., Matteppanavar, S., Rayaprol, S., Babu, P.D., Pasha, U.M.: Structural, electronic and magnetic properties of Sc3+doped CoCr2O4 nanoparticles. New J. Chem. **44**, 14246–14255 (2020). https://doi.org/10.1039/d0nj03062g

38. Pawar, R.A., Patange, S.M., Shitre, A.R., Gore, S.K., Jadhav, S.S., Shirsath, S.E.: Crystal chemistry and single-phase synthesis of Gd3+ substituted Co-Zn ferrite nanoparticles for enhanced magnetic properties. RSC Adv. **8**, 25258–25267 (2018). https://doi.org/10.1039/c8ra04282a

39. Meiklejohn, W.H., Bean, C.P.: New magnetic anisotropy. Phys. Rev. **102**, 1413–1414 (1956). https://doi.org/10.1103/PhysRev.102.1413

40. Santiago, A.A.G., Tranquilin, R.L., Oliveira, M.C., Ribeiro, R.A.P., De Lazaro, S.R., Correa, M.A., Bohn, F., Longo, E., Motta, F.V., Bomio, M.R.D.: Disclosing the structural, electronic, magnetic, and morphological properties of CuMnO2: a unified experimental and theoretical approach. J. Phys. Chem. C. **124**, 5378–5388 (2020). https://doi.org/10.1021/acs.jpcc.0c00198

41. Rostami, M., MajlesAra, M.H.: The dielectric, magnetic and microwave absorption properties of Cu-substituted Mg-Ni spinel ferrite-MWCNT nanocomposites. Ceram. Int. **45**, 7606–7613 (2019). https://doi.org/10.1016/j.ceramint.2019.01.056

42. Xu, D., Jafarian, M., Seyyed Afghahi, S.S., Atassi, Y., Bani Al-Marjeh, R.A.Q.: Remarkable microwave absorption efficiency of low loading ratio of Ni0.25Co0.25Ti0.5Fe2O4/SrCoTiFe10O19/Cu composite coated with polyprrole within polyurethane matrix. Mater. Res. Express. **7**, 0–10 (2019). https://doi.org/10.1088/2053-1591/ab62f1

43. Yang, W., Zhang, Y., Qiao, G., Lai, Y., Liu, S., Wang, C., Han, J., Du, H., Zhang, Y., Yang, Y., Hou, Y., Yang, J.: Tunable magnetic and microwave absorption properties of Sm1.5Y0.5Fe17-xSix and their composites. Acta Mater. **145**, 331–336 (2018). https://doi.org/10.1016/j.actamat.2017.12.042

44. Bsoul, I., Mahmood, S.H., Lehlooh, A.F., Al-Jamel, A.: Structural and magnetic properties of SrFe12-2xTixRuxO19. J. Alloys Compd. **551**, 490–495 (2013). https://doi.org/10.1016/j.jallcom.2012.11.062

45. Stoner, B.E.C.: A mechanism of magnetic hysteresis in heterogeneous alloys. **826**, 599–642 (1948)

46. Liu, P., Ng, V.M.H., Yao, Z., Zhou, J., Lei, Y., Yang, Z., Kong, L.B.: Microwave absorption properties of double-layer absorbers based on Co0.2Ni0.4Zn0.4Fe2O4 ferrite and reduced graphene oxide composites. J. Alloys Compd. **701**, 841–849 (2017). https://doi.org/10.1016/j.jallcom.2017.01.202

47. Qian, K., Yao, Z., Lin, H., Zhou, J., Haidry, A.A., Qi, T., Chen, W., Guo, X.: The influence of Nd substitution in Ni–Zn ferrites for the improved microwave absorption properties. Ceram. Int. **46**, 227–235 (2020). https://doi.org/10.1016/j.ceramint.2019.08.255

48. Vinnik, D.A., Klygach, D.S., Zhivulin, V.E., Malkin, A.I., Vakhitov, M.G., Gudkova, S.A., Galimov, D.M., Zherebtsov, D.A., Trofimov, E.A., Knyazev, N.S., Atuchin, V.V., Trukhanov, S.V., Trukhanov, A.V.: Electromagnetic properties of BaFe12O19: Ti at centimeter wavelengths. J. Alloys Compd. **755**, 177–183 (2018). https://doi.org/10.1016/j.jallcom.2018.04.315

49. El Shater, R.E., El-Ghazzawy, E.H., El-Nimr, M.K.: Study of the sintering temperature and the sintering time period effects on the structural and magnetic properties of M-type hexaferrite BaFe12O19. J. Alloys Compd. **739**, 327–334 (2018). https://doi.org/10.1016/j.jallcom.2017.12.228

50. Kumar, S., Supriya, S., Pandey, R., Pradhan, L.K., Singh, R.K., Kar, M.: Effect of lattice strain on structural and magnetic properties of Ca substituted barium hexaferrite. J. Magn. Magn. Mater. **458**, 30–38 (2018). https://doi.org/10.1016/j.jmmm.2018.02.093

51. Anjum, S., Seher, A., Mustafa, Z.: Effect of La3+ ions substituted M-type barium hexa-ferrite on magnetic, optical, and dielectric properties. Appl. Phys. A Mater. Sci. Process. **125**, (2019). https://doi.org/10.1007/s00339-019-2937-6